Interfacial charge transfer in functionalized multi-walled carbon nanotube@TiO$_2$ nanofibres†

Avishek Saha, [iD] ‡[a] Alicia Moya,‡[b] Axel Kahnt, [iD] [a] Daniel Iglesias,[c]
Silvia Marchesan, [iD] [c] Reinhold Wannemacher,[d] Maurizio Prato,[c,e,f] Juan J. Vilatela*[b]
and Dirk M. Guldi [iD] *[a]

A new insight into photoinduced charge transfer processes across carbon nanotube@TiO$_2$ interfaces has been gained based on experimental details from transient absorption spectroscopy. We show that photo-induced, interfacial hole transfer to carboxylic acid-functionalized multiwalled carbon nanotubes (oxMWCNTs) from TiO$_2$ results in hole-doped oxMWCNTs and reduced TiO$_2$. The latter is inferred from femto- and nanosecond transient absorption spectroscopy performed with oxMWCNT@TiO$_2$ dispersions and complemented with investigations using methyl viologen and N,N,N′,N′-tetramethyl-p-phenylene-diamine as an electron scavenger and a hole scavenger, respectively. The results of ultraviolet photo-emission spectroscopy (UPS) of the compounds corroborate the findings, highlighting the strong coupling between oxMWCNTs and TiO$_2$ in these hybrids.

Introduction

Titanium dioxide unique photocatalytic properties have led research groups around the globe to design novel and more efficient photocatalytic systems.[1–4] For example, nano-sized TiO$_2$ has extensively been studied due to the synergy stemming from a high specific surface area, large availability of reaction sites, as well as the possibility of obtaining diverse morphologies. Notable are fibres,[5,6] thin films,[7] rods,[8,9] platelets[10,11] or opals[11] with properties different from bulk materials. Mesoporous nanostructured TiO$_2$ architectures are of particular interest owing to their large surface-to-volume ratios and networks of interconnected crystals.

As such, not only interfacial charge transfer but also longer diffusion lengths of charge carriers are facilitated.[12–22]

[a]Department of Chemistry & Pharmacy and Interdisciplinary Center for Molecular Materials, Friedrich Alexander University Erlangen-Nuremberg, Egerlandstrasse 3, 91058 Erlangen, Germany. E-mail: guldi@fau.de

[b]IMDEA Materials Institute, Eric Kandel 2, Getafe, Madrid, 28906, Spain. E-mail: juanjose.vilatela@imdea.org

[c]Center of Excellence for Nanostructured Materials INSTM, Unit of Trieste Dipartimento di Scienze Chimiche e Farmaceutiche Università degli Studi di Trieste, Via Giorgieri 1, 34127 Trieste, Italy

[d]Madrid Institute for Advanced Studies, IMDEA Nanoscience, C/Faraday 9, Campus Cantoblanco, 28049 Madrid, Spain

[e]Carbon Nanobiotechnology Laboratory, CIC biomaGUNE, Paseo de Miramón 182, 20009 Donostia-San Sebastian, Spain

[f]BasqueFdnSci, Ikerbasque, Bilbao 48013, Spain

‡These authors contributed equally to this work.

Additional benefits of TiO$_2$ come from charge separation between anatase and rutile due to differences in their electronic structures.[13–15] Durrant and coworkers have, for example, demonstrated that hole transfer from anatase to rutile contributes to the photocatalytic enhancement in mesoporous anatase/rutile heterojunctions.[14]

A complementary strategy to yield higher photocatalytic efficiencies consists of promoting charge separation by hybridization of TiO$_2$. At the forefront of investigations are metals,[16–18] metal oxides,[19,20] and non-metals such as nitrogen,[21,22] sulphur,[23] carbon,[24,25] etc. Besides the aforementioned atomic dopants, nanocarbons are emerging as a molecular dopant to hybridize TiO$_2$.[26–30] Importantly, an increase in photocatalytic activity by a factor of up to 4 compared to bare TiO$_2$ nanoparticles has been reported.[31] The overall increase in the photocatalytic activity of TiO$_2$ upon addition of nanocarbons has been attributed to (i) better charge separation across the interface with longer photo-carrier lifetimes,[26] (ii) larger surface areas in combination with other relevant morphological effects, and (iii) photosensitization by nanocarbons.[31] Such enhanced, interfacial charge transfer processes in nanocarbon hybrids have been exploited in several other energy-related applications, such as photo (electro)catalysis, batteries and supercapacitors or sensing.[32]

Despite the undisputed importance of charge transfer across nanocarbon@TiO$_2$ interfaces, the nature and the dynamics of photoexcited charge-carriers in these hybrid systems remain unclear. Even the directionality of charge transfer, a basic step to elucidate further progress of the photo-catalytic reaction, is ambiguous. Interestingly, it has been

documented that carbon nanotubes facilitate both hole and electron extraction in photovoltaic devices.[33–36] In the context of photocatalysis, Woan *et al.* proposed, for example, a pathway, which involves an electron transfer from TiO_2 to multi-walled carbon nanotubes (MWCNTs) under UV light irradiation.[29] In sharp contrast, electron transfer to TiO_2 has been reported upon covalently linking single-walled carbon nanotubes (SWCNTs) and in TiO_2-SWCNT dye sensitised solar cells.[37,38] Recent photo-electrochemical studies suggest that when combined with ZnO, which has similar band positions to TiO_2, MWCNTs may act as a hole acceptor and, in turn, increase the current conversion efficiencies.[39] Such discrepancies are partly ascribable to differences in interfacing nanocarbon and metal oxides. Simple mixing, on the one hand, produces a composite with two distinct phases. *In situ* growth of the metal oxide in the presence of nanocarbons, on the other hand, leads to the formation of hybrids. The properties of the latter are dominated in some instances by interfacial processes and new interfacial energy states.[40] Additionally, the systems under photocatalytic study often contain Pt, which has a strong effect on charge transfer dynamics.

In this context, we have investigated the directionality and dynamics of charge transfer across interfaces in mesoporous MWCNT@TiO_2 hybrids. They have been produced by a combination of sol–gel and electrospinning and have recently been shown to have high photocatalytic activity towards hydrogen production.[28] The large interfaces between nanocarbons and semiconducting metal oxides render the resulting hybrids ideal to study interfacial charge transfer processes – an approximation of the interface is given in the ESI.†

Importantly, MWCNT@TiO_2 hybrids are uniquely suitable for charge transport measurements either in the form of single fibres,[41,42] or sintered electrodes.[43] Also, their application as dispersions for photocatalytic reactions is notable. Through a combination of transient absorption spectroscopy and photocatalytic test reactions, we demonstrate interfacial charge separation in these hybrids and provide rates for the different processes. The dominant mechanism is most likely based on a hole transfer from TiO_2 to MWCNT under UV photoexcitation.

Results and discussion

Fig. 1 presents electron micrographs of the mesoporous TiO_2 materials used in this study. They consist of uniform fibres with rough surfaces and a diameter of 300 ± 100 nm (Fig. 1a). At higher magnification, the TEM images (Fig. 1b) corroborate that the fibres feature TiO_2 crystalline domains with an average size of 12 nm. These are interconnected along the fibre structure yet giving rise to pores with sizes in the mesoporous range.[28] The addition of oxMWCNTs in the range of concentrations from 1 to 5 vol% does not change the overall mesoporosity. By virtue of growing TiO_2 *in situ*, the presence of oxMWCNTs generates large oxMWCNT@TiO_2 interfaces, where the two components are in close proximity (Fig. 1c). From the electron diffraction (ED) pattern, we derive the pres-
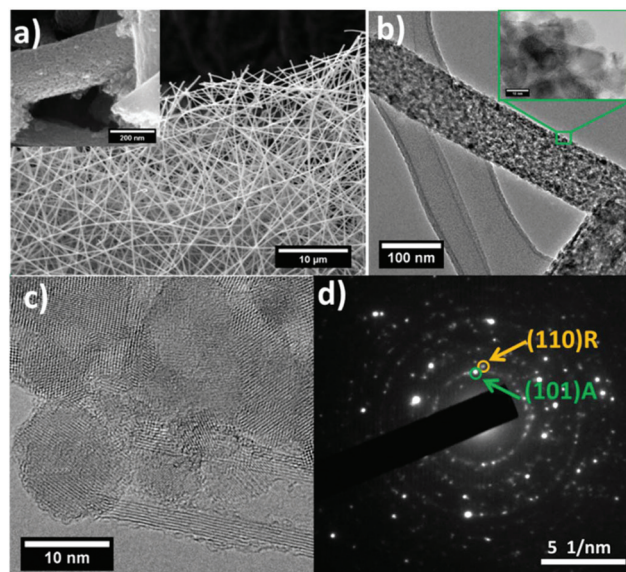

Fig. 1 (a) SEM image of TiO_2 nanofibres with the inset showing an individual microscopic fibre. (b) TEM image of oxMWCNT@TiO_2 fibres with an inset that shows the interconnection of TiO_2 nanocrystals. (c) HRTEM image of crystalline TiO_2 nanocrystals interfacing with oxMWCNTs. (d) ED pattern corresponding to (b).

ence of anatase (A) and rutile (R) (Fig. 1d). From XRD measurements the A/R ratio is found to be 0.7. Anatase to rutile phase transformation occurs usually above 500 °C using sol–gel methods although a low temperature transformation is plausible.[44] In our synthetic route, the large nanocrystal surface and the use of an inert atmosphere accelerate this process.[28] Overall, the benefit of the combined sol–gel/electrospinning method used here is the formation of a mesoporous nanocrystalline TiO_2 structure containing uniformly dispersed oxMWCNTs forming a tight interface.[28]

Next, the TiO_2 fibres were characterized by Raman spectroscopy to determine compositional features as they may exert an impact on the photocarrier dynamics – *vide infra*. Representative spectra for electrospun bare TiO_2 and 5 vol% ox-MWCNT@TiO_2 are presented in Fig. 2. In addition, the Raman spectrum of TiO_2 nanoparticles produced by a standard sol–gel method lacking the mesoporous structure arising from the combined sol–gel/electrospinning process is shown. The Raman modes of the anatase phase are clearly visible: 144 cm^{-1} (E_g), 197 cm^{-1} (E_g), 399 cm^{-1} (B_{1g}), 515 cm^{-1} (A_{1g}) superimposed onto 519 cm^{-1} (B_{1g}) and 639 cm^{-1} (E_g). The presence of the rutile phase is confirmed by Raman modes at 447 cm^{-1} (E_g) and 612 cm^{-1} (A_{1g})[45] and XRD (Fig. S3†).

In Fig. 2a, the peak at 144 cm^{-1} is shifted and wider in the fibres compared to that for nanoparticles produced by sol–gel. The 144 cm^{-1} peak corresponds to vibrations of the Ti–O skeleton in the anatase phase and its high intensity suggests the long-range order of anatase crystals produced during annealing. A shifting and broadening infers the existence of oxygen vacancies in the TiO_2 structure. Thus, combining a sol–gel process and electrospinning as part of the low temperature
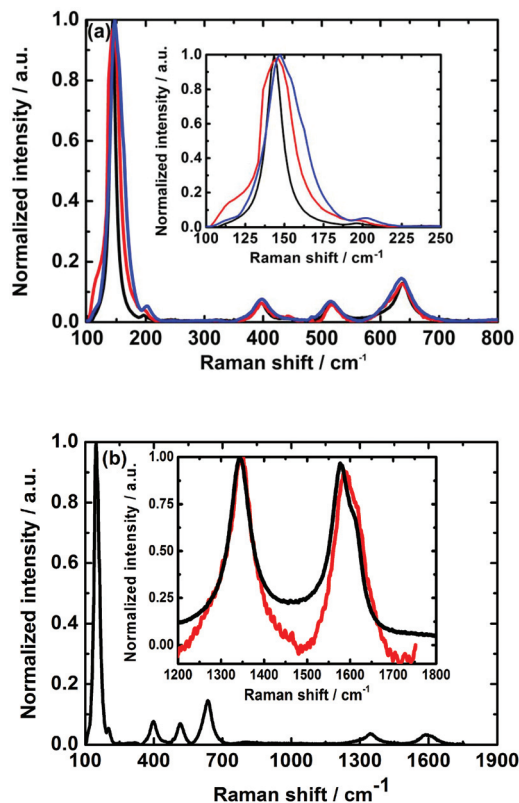
Fig. 2 (a) Raman spectra of TiO$_2$ nanoparticles (black spectrum), TiO$_2$ fibres (red spectrum), and 5 vol% oxMWCNT@TiO$_2$ (blue spectrum). The inset shows the zoom into the 100−250 cm^{-1} region. (b) Extended Raman spectrum of 5 vol% oxMWCNT@TiO$_2$, the inset shows D and G peaks of oxMWCNTs before (black spectrum) and after hybridization with TiO$_2$ (red spectrum).

synthetic route followed by annealing under an inert atmosphere favours the existence of defects in the electrospun fibres. Such oxygen vacancies are likely the inception leading to interfacial sharing between neighbouring TiO$_2$ nanocrystals, resulting in stronger interactions between them. The chemical contact between crystals is thought to outweigh the negative effect of vacancies acting as electron traps and delaying charge transfer processes. Interestingly, the largest shifts were observed for oxMWCNT@TiO$_2$, which suggests that oxMWCNTs induce additional distortion to the TiO$_2$ structure, for example, through the formation of a Ti–O–C interfacial bond, predicted to have a formation energy of −1.74 eV.[28,46]

Fig. 2b shows the extended Raman spectrum of the 5 vol% oxMWCNT@TiO$_2$ hybrid. In the low wavenumber range, the signatures of the anatase phase are discernible. In the high wavenumber range, the presence of the D and G bands of oxMWCNTs at 1345 and 1594 cm^{-1}, respectively, confirms that the hybridization leaves the oxMWCNTs intact. More importantly, an 18 cm^{-1} upshift in the G band is seen to evolve from the hybridization (Fig. 2b). Shifts in Raman modes are often due to mechanical strain.[47] A likely source would be the annealing treatment, where a densification of the Ti network could induce a compression in the oxMWCNTs. Such a mech-

anical effect would, however, broaden the G band and produce a small displacement in the D band.[48] Neither broadening nor D band upshifting is observed. An alternative source is doping of oxMWCNTs.[49] To this end, oxMWCNT hybridization, that is, the growth of TiO$_2$ nanocrystals, might alter the electronic structure of oxMWCNTs *via* the possible formation of C–O–Ti bonds. Independent confirmation of our hypothesis comes from hybrids produced by other synthetic methods and will be reported in future work.

The photoluminescence (PL) of TiO$_2$ and oxMWCNT@TiO$_2$ fibres spans the spectral range from 400 to 600 nm. It is composed of different contributions (Fig. 3). In the high-energy region, the PL corresponds to the indirect band-to-band recombination across the band gap (red line). PL in the low energy range is attributed to excitons (green line), which result
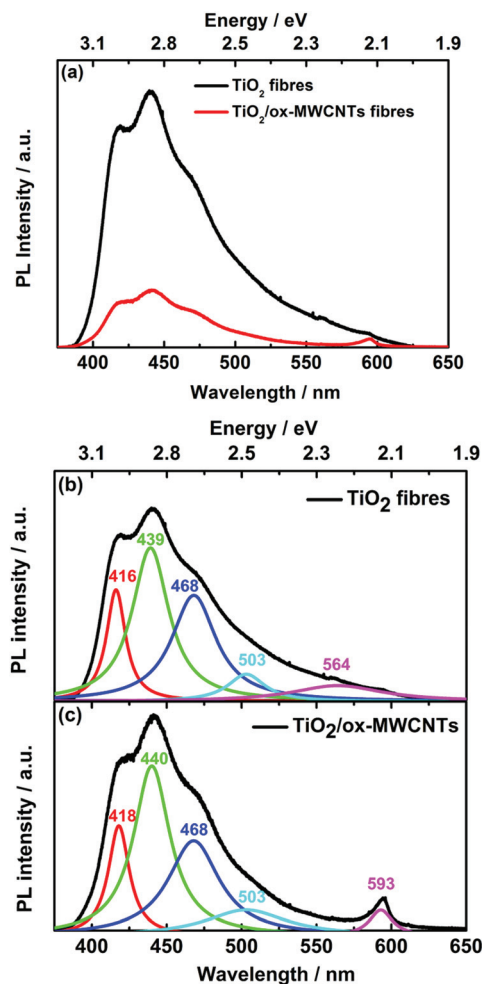

Fig. 3 (a) Photoluminescence spectra of TiO$_2$ (black) and 5 vol% oxMWCNT@TiO$_2$ (red) upon 355 nm excitation. (b) Lorentzian fitting of the emission band of the TiO$_2$ fibres corresponding to the contribution of indirect band-to-band recombination (red), excitons (green), trapped electrons from defects and O vacancies (blue and cyan) and trapped holes (magenta). (c) Lorentzian fitting of the emission band of 5 vol% oxMWCNT@TiO$_2$ corresponding to the contribution of indirect band-to-band recombination (red), excitons (green), trapped electrons from defects and O vacancies (blue and cyan) and trapped holes (magenta).

from surface oxygen vacancies and defects (blue and cyan lines), which is consistent with Raman analyses. The 600 nm PL maximum (magenta line) is assigned to the recombination of electrons with holes trapped in states above the valence band.[50] Considering that this peak is more pronounced in the hybrids, we conclude that hybridization with MWCNTs is likely to be linked to the formation of new intra-band gap states. Moreover, Fig. 3 documents a quenching of the PL by 75% in the 5 vol% oxMWCNT@TiO$_2$ hybrid in comparison with TiO$_2$ fibres. As such, oxMWCNTs facilitate the charge separation across the oxMWCNT@TiO$_2$ interface, which delays the electron–hole recombination.[51]

Combined ultraviolet photoemission spectroscopy (UPS) and X-ray photoemission spectroscopy (XPS) provides insights into the electronic structure and energy band positions of the different materials. With their work function at hand, we gather information regarding a possible charge injection barrier at the ox-MWCNTs@TiO$_2$ interfaces. Fig. 4a shows the full spectra of the 5 vol% oxMWCNTs@TiO$_2$ and individual components, TiO$_2$ and oxMWCNTs. A clear difference in the UPS spectra with the secondary electron cut-off and the valence band edge shifted to lower binding energies is observed in oxMWCNTs@TiO$_2$ in comparison with TiO$_2$. From the secondary cut-off at high binding energy, represented in

Fig. 4 (a) UPS spectra of TiO$_2$, oxMWCNTs, and 5 vol% oxMWCNT@TiO$_2$. (b) UPS spectra of the secondary electron with the onset highlighted in the graph to determine the work function. (c) Valence band edge of UPS spectra.

Fig. 4b, the work function (φ) was determined by subtracting the cut-off energy from the photon energy (21.2 eV). The work function calculated for the TiO$_2$ fibres and oxMWCNTs@TiO$_2$ is 4.32 and 4.37 eV, respectively, in agreement with the literature values for anatase nanostructures.[52] Minor differences of 0.05 eV are observed in the work function of both materials and the changes suggest band bending during the hybridisation of TiO$_2$ with oxidized MWCNTs which have a higher work function (4.7 eV).

We note that the literature values for the work function of CNTs range from 4.3[53] to 5.6 eV,[54] whereas for TiO$_2$ they span from 4 to 5.1 eV.[55,56] Such a wide range renders it rather difficult to predict a generic band alignment in oxMWCNT@TiO$_2$, but confirms that the interfacial charge transfer processes proposed below are entirely plausible. From the low binding energy region (Fig. 4c), the positions of the valence band maxima (VBM) are derived as the intercepts between the tangents of the spectra and the baseline. The ionization energy is 7.46 eV, in agreement with the reported values.[57] Noticeable differences are observed in the edge of the valence band states in oxMWCNT@TiO$_2$. A continuous distribution of valence band states is measured up to ~1.72 eV with respect to the Fermi level, corresponding to an ionization energy of 6.09 eV. This suggests the presence of states within the band gap of the hybrid. These states are presumably formed at the oxMWCNT@TiO$_2$ interface and will give rise to hole transport as a dominant mode of charge transfer across the oxMWCNT@TiO$_2$ interface.[58] Moreover, the UPS measurements place the ionization energy of oxMWCNT at 5.51 eV, which, being much smaller than the corresponding value for TiO$_2$ (7.46 eV), clearly suggests a transfer of holes from TiO$_2$ to oxMWCNT.[47]

Predicting the directionality of charge transfer requires precise insights into the interfacial chemistry, structure and energy states.[59–62]

The morphology of electrospun oxMWCNT@TiO$_2$ consists of a network of TiO$_2$ nanocrystals (12 nm) and immobilized MWCNTs. These hybrids are best characterised by a large interfacial region resulting from *in situ* growth of TiO$_2$ onto oxMWCNTs. At the interface, specific chemical features, such as Ti–O–C bonds or physical adsorptions of TiO$_2$ at carboxylic sites (see XPS spectra in Fig. S4†), are expected to produce local changes in the electronic structure and most likely new interfacial energy states.[46,63–65] From the UPS spectra shown in Fig. 4c we infer that the valence band region of oxMWCNT@TiO$_2$ is shifted to lower binding energies compared with bare TiO$_2$ and resembles that of MWCNTs. We take the aforementioned inference as evidence for strong interactions and charge transfer across the interface between oxMWCNT and TiO$_2$.

The emergence of PL, again, might reflect the presence of interfacial states specific to oxMWCNT@TiO$_2$. Ultimately, the Raman and photoelectron emission spectroscopy characterisation highlight the fact that the oxMWCNT@TiO$_2$ fibres are a hybrid material, distinctly different from its components and with electronic properties emerging from large interfacial regions. Most importantly, the formation of covalent bonds at
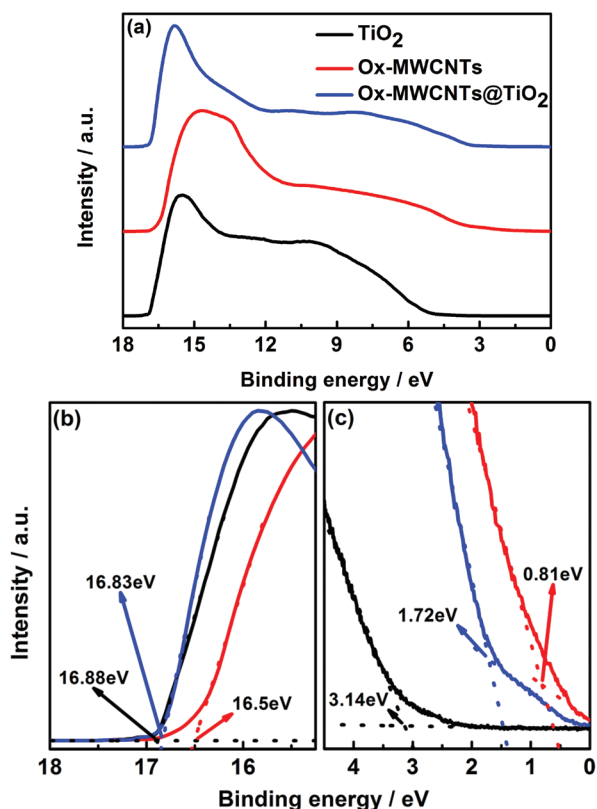
the oxMWCNT@TiO$_2$ interface is expected to favour interfacial charge transfer.

To understand the dynamics of photoexcited states, we turned to transient absorption spectroscopy (TAS), a useful technique to monitor the separation of electron–hole pairs in TiO$_2$ materials.[66,67] Fig. 5 shows femtosecond-transient absorption spectra with time delays of 2–500 ps for TiO$_2$ nanofibres deposited on quartz slides upon 258 nm excitation. The laser excitation power was chosen in the range of 250–600 nJ per pulse to prevent nonlinear processes. We noted two significant features, that is, negative transients in the visible region and positive broad transients in the NIR region. We further observed increases in the intensity of the NIR transients, which is caused by the absorption of free conduction band electrons. It proved, however, difficult to detect evidence for trapped holes in the form of a broad positive band at 520 nm as reported by Yoshihara *et al.*[68] in the case of nanocrystalline anatase TiO$_2$ films. These authors observed hole trapping in the range of microseconds, while others have reported sub-ps time scales for the rise and decay of differential absorptions at λ = 520 nm in colloidal anatase nanoparticles and ascribed these transients to shallow trapped holes.[69,70] Notably, the
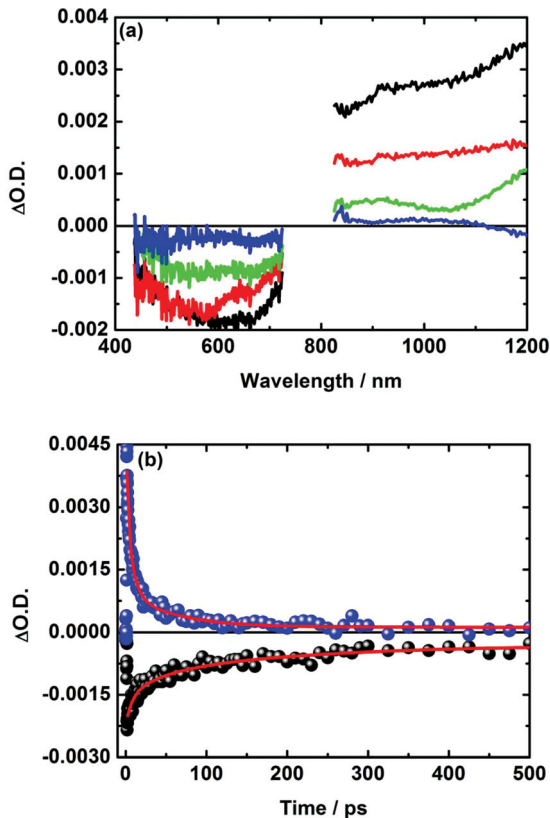
transient absorption spectra regarding hole trapping depends on factors such as TiO$_2$ morphology, excitation wavelengths, pump energy density, *etc.*[70,71] In the context of our measurements, the negative transients in the visible region cannot be ascribed to bleaching of ground state absorption upon photoexcitation, since TiO$_2$ does not absorb in this particular wavelength region. In order to exclude instrumental artefacts, we performed femtosecond laser photolysis transient absorption on thin films made from TiO$_2$ nanoparticles (Solaronix). In these reference experiments, we noted positive transients in both visible and near-IR regions immediately after 258 nm photoexcitation with femtosecond laser pulses – Fig. S5.†

The absence of transient absorptions due to the holes localised in TiO$_2$ might relate to two aspects. On the one hand, an ultrafast hole relaxation, and, on the other hand, masking of the hole absorption signatures by the strong negative signals in the visible region most likely is due to stimulated emission. The kinetics in the visible and NIR regions at 600 and 1000 nm, respectively, could be fitted with a three-exponential fitting function with a short-lived component ranging from 3 to 6 ps, an intermediate component between 35 and 55 ps, and a long-lived component of around 350 ps – Fig. 5b. The short-lived and the long-lived components in the NIR region could be assigned to relaxation of trapped electrons from shallow and deep traps, respectively. The presence of charge traps in our TiO$_2$ is confirmed by photocurrent measurements on individual TiO$_2$ fibres, which show strong photo-gating effects, most likely associated with electrons immobilized in O-vacancies or in other charge traps.[42]

In the case of the oxMWCNT@TiO$_2$ hybrids, distinct changes evolve in the transient absorption spectra, that is the appearance of broad transients around 700 nm – Fig. 6 and 7. Importantly, the transients throughout the NIR decay with similar time constants. Bahnemann *et al.* reported that the absorption of electron-abundant TiO$_2$ results in a broad peak at around 650 nm.[67] We therefore tentatively assign the 700 nm feature to trapped electrons residing in TiO$_2$.

Turning to the entire NIR transient, we hypothesize contributions from two components: On the one hand, hole doped oxMWCNTs, and, on the other hand, trapped electrons on TiO$_2$. If our first assumption is correct, the rise time of the NIR transients should reflect the timescale of interfacial charge separation. Table S1† summarizes the time constants including pre-exponential factors of the exponential fittings determined by analysing time absorption profiles at different wavelengths. For example, the lifetime of the NIR transients of 1 vol% oxMWCNTs is nearly three times larger than bare TiO$_2$ – Fig. 6b. We infer from the latter that the presence of 1 vol% oxMWCNTs slows down the electron–hole recombination, when considering both assignments of the transients. Further increasing the amount of oxMWCNTs up to 5 vol% failed to suppress the electron–hole recombination although we observed longer lifetimes of the transients related to trapped electrons at 700 nm – Fig. 7b.

To probe the charge recombination dynamics on longer timescales, we employed nanosecond transient absorption
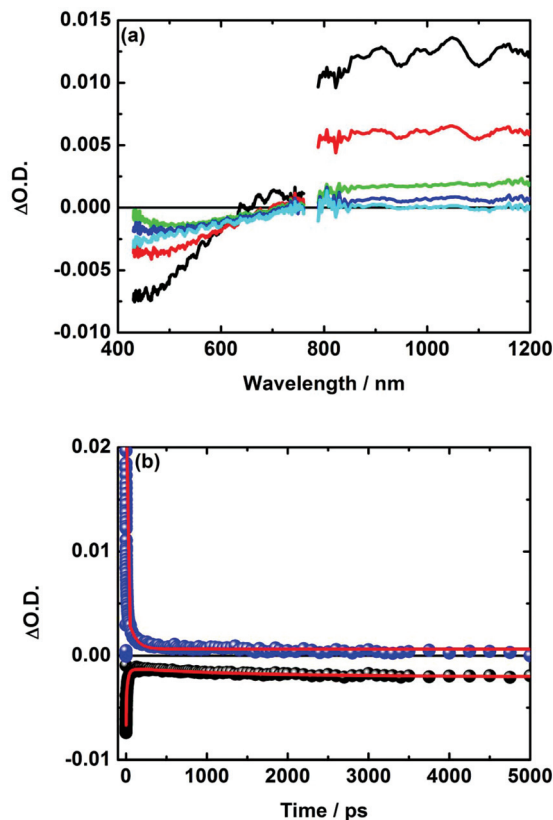

Fig. 5 (a) Femtosecond laser photolysis transient absorption spectra of TiO$_2$ nanofibers deposited on quartz slides upon photoexcitation at 258 nm (~250 nJ per pulse, 150 fs FWHM) with time delays of 2 ps (black), 10 ps (red), 50 ps (green), and 500 ps (blue). Visible and Near-IR spectra were recorded at different spots. (b) Corresponding absorption time profiles at 600 nm (black) and 1000 nm (blue). The fits are depicted in red.

Fig. 6 (a) Femtosecond laser photolysis transient absorption spectra of 1 vol% oxMWCNT@TiO$_2$ nanofibers upon photoexcitation at 258 nm (~250 nJ per pulse, 150 fs FWHM) with time delays of 2 ps (black), 10 ps (red), 100 ps (green), 100 ps (blue) and 5000 ps (cyan). Visible and Near-IR spectra were recorded at different spots. (b) Corresponding absorption time profiles at 500 nm (black) and 1000 nm (blue). The fits are depicted in red.
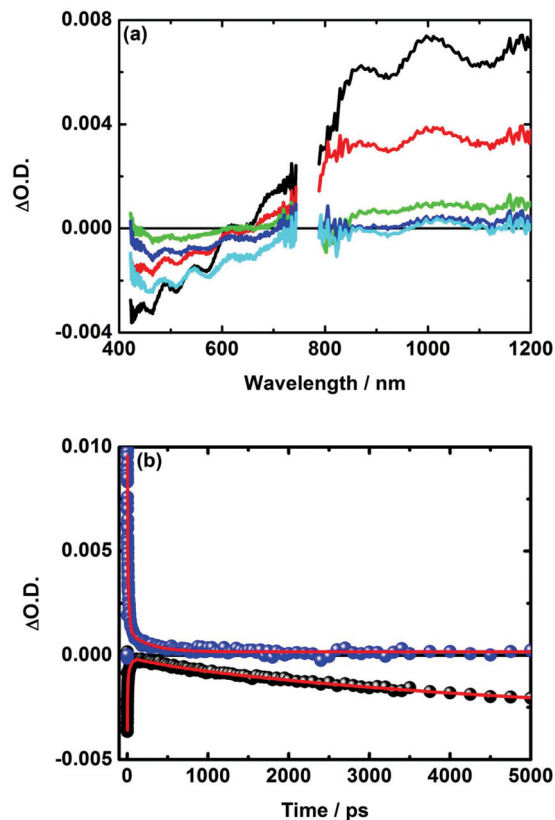
Fig. 7 (a) Femtosecond laser photolysis transient absorption spectra of 5 vol% oxMWCNT@TiO$_2$ nanofibers upon photoexcitation at 258 nm (~250 nJ per pulse, 150 fs FWHM) with time delays of 2 ps (black), 10 ps (red), 100 ps (green), 100 ps (blue) and 5000 ps (cyan). Visible and Near-IR spectra were recorded at different spots. (b) Corresponding absorption time profiles at 500 nm (black) and 1000 nm (blue). The fits are depicted in red.

spectroscopy. Fig. S6† shows nanosecond transient absorption spectra of colloidal dispersion of bare TiO$_2$ nanofibers in D$_2$O. Here, we observed negative differential absorptions at 30 ns below 450 nm.[72] These transform into weak positive transients after *ca.* 30 ns – see Fig. S6.† The NIR lacks any appreciable transient absorption changes on the nanosecond timescale. Even in the absence of probe light, we observed negative transient signals with a lifetime of 23 ns as shown in Fig. S7.† From the latter, we deduce contributions from PL to the overall negative signal in a range beyond the bandgap of TiO$_2$.

In contrast to TiO$_2$, both 1 vol% oxMWCNT@TiO$_2$ and 5 vol% oxMWCNT@TiO$_2$ show positive transient absorption signals in the NIR region – Fig. 8. This indicates the appearance of new transients upon photoexcitation of the oxMWCNT@TiO$_2$ nanohybrids at 355 nm. Considering that bare TiO$_2$ does not produce any NIR transients on the nanosecond timescale, it indicates that the transients in oxMWCNT@TiO$_2$ are related to longer lived charge separated states. As far as the dynamics are concerned, the transients of 1 vol% oxMWCNT@TiO$_2$ and 5 vol% oxMWCNT@TiO$_2$ hybrids at 800 nm yield time constants of 60 and 75 ns,

respectively. In other words, increasing the amount of oxMWCNTs assists in stabilizing the product of charge separation and suppressing charge recombination.

To gain more insights into the nature of the NIR transients, quenching experiments using methyl viologen (MV, E_{red} = −0.44 V *vs.* NHE) as an electron acceptor and *N,N,N′,N′*-tetramethyl-*p*-phenylenediamine (TMPD, E_{ox} = +0.25 V *vs.* NHE, first oxidation) as a hole acceptor have been performed.[73,74] In our first photocatalytic experiments, oxMWCNT@TiO$_2$ acts as an electron donor to reduce the methyl viologen cation (MV^{2+}) to the corresponding methyl viologen radical cation (MV$^{•+}$) and, in turn, resulting in a blue colour. Indeed, our steady state absorption assays give rise to an absorption, which maximizes at around 600 nm, and, which corresponds to MV$^{•+}$.[75] Please note that the reduction of MV^{2+} is thermodynamically only feasible with electrons from the conduction bands of TiO$_2$ and, according to UPS data, this is placed at −0.18 V *vs.* NHE (pH 0), limiting thus the photocatalytic process.[76] However, at pH higher than 4.4, the TiO$_2$ conduction band is suitable for photocatalytic reduction of MV^{2+} and therefore, our experiments were performed at pH 7.0 ± 0.2. To this end,
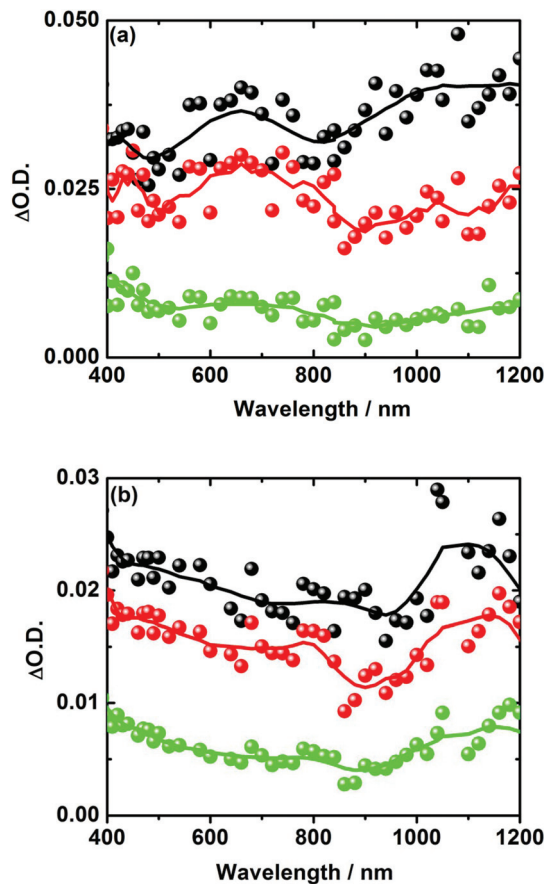
Fig. 8 Nanosecond transient absorption spectra recorded upon 355 nm photoexcitation (~8 mJ per pulse, 5 ns FWHM) of dispersion of (a) 1% oxMWCNT@TiO$_2$ and (b) 5% oxMWCNT@TiO$_2$ in D$_2$O with time delays of 75 ns (black), 100 ns (red), and 150 ns (green).
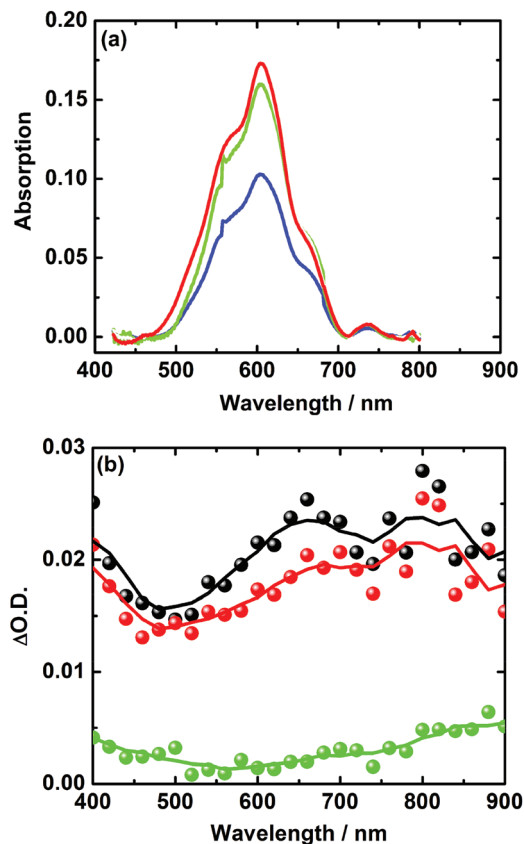
Fig. 9 (a) Steady state absorption spectra of a methyl viologen radical cation in the presence of TiO$_2$ (blue spectrum), 1 vol% oxMWCNT@TiO$_2$ (green spectrum), and 5 vol% oxMWCNT@TiO$_2$ (red spectrum) dispersions in D$_2$O after irradiation with a 302 nm 6 W UV lamp for 20 minutes. (b) Nanosecond laser photolysis transient absorption spectra recorded upon 355 nm photoexcitation (~8 mJ per pulse, 5 ns FWHM) of 1 vol% oxMWCNT@TiO$_2$ dispersions with 1 mM [MV]Cl$_2$− in D$_2$O with time delays of 75 ns (black), 100 ns (red), and 200 ns (green).

Fig. 9a shows the baseline subtracted cw absorption spectra of MV$^{\bullet+}$ in the presence of TiO$_2$ and oxMWCNT@TiO$_2$ with different oxMWCNT volume fractions. In comparison with bare TiO$_2$, the peak intensity is higher for oxMWCNT@TiO$_2$. This correlates with higher concentrations of MV$^{\bullet+}$, which have been produced. It is fair to conclude that the photocatalytic reduction of MV^{2+} is more efficient in the presence of oxMWCNT. It reflects an enhanced interfacial charge separation in oxMWCNT@TiO$_2$ upon light exposure. Interestingly, much longer lived MV$^{\bullet+}$ was reported in the presence of TiO$_2$ nanoparticles,[73] which infers a faster charge recombination with hole doped oxMWCNTs.

For example, in nanosecond transient absorption spectra longer charge recombination (72 ns, Fig. 9b) is noted in the presence of 1 mM MV^{2+} in D$_2$O. Most likely, the longer-lived NIR transients are related to the interaction between reduced MV$^{\bullet+}$ and oxidized oxMWCNTs, since transients from trapped/conduction band electrons on TiO$_2$ should decay faster in the presence of an electron scavenger. Graetzel *et al.* reported that the dynamics of photoexcited electron transfer from TiO$_2$ conduction bands to MV^{2+} depends on the initial MV^{2+} concentration and the pH of the dispersion.[77]

On the other hand, the nanosecond transient absorption spectra of 1 vol% oxMWCNT@TiO$_2$ in the presence of *N,N,N′,N′*-tetramethyl-*p*-phenylenediamine (TMPD) show a 21 μs lived transient at 600 nm and weak transients in the NIR region – Fig. 10. This is rationalized on the basis of hole scavenging in the form of TMPD to generate the TMPD radical cation, which, in turn, renders hole-doped oxMWCNT shorter-lived than in the absence of TMPD. As such, the 21 μs lived transients are related to the TMPD radical cation. An obvious question arises relating to TMPD access to the interface of oxMWCNTs. It is important to note that we conclude from the TEM images that oxMWCNTs are not entirely coated with TiO$_2$. Furthermore, TMPD might access the sidewalls of oxMWCNTs through the porous network of the TiO$_2$ fibres. Taking the aforementioned fact into account, TMPD withdraws holes from oxMWCNTs.

In summary, taking all our experimental findings into account, we gathered strong evidence for a hole transfer mechanism from the TiO$_2$ valence band as the dominant interfacial process upon photoexcitation. A scheme of the hole transfer is depicted in Fig. 11.
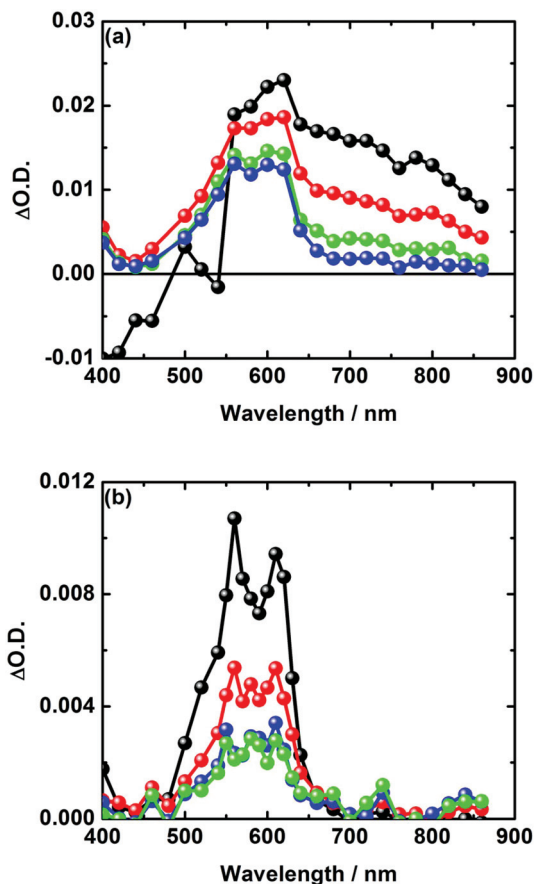
Fig. 10 Nanosecond laser photolysis absorption spectra recorded upon 355 nm excitation (~8 mJ per pulse) of 1 vol% oxMWCNT@TiO$_2$ dispersions with ~20 mM TMPD in D$_2$O with time delays of (a) 60 ns (black), 150 ns (red), 250 ns (green), and 350 ns (blue) and with time delays of (b) 1 μs (black), 20 μs (red), 50 μs (blue), and 75 μs (green).
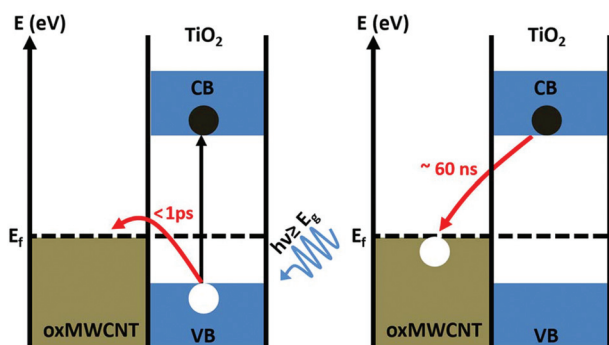

Fig. 11 Schematic illustration of the ultrafast photoinduced hole transfer from the TiO$_2$ valence band to oxMWCNTs and the charge recombination upon 258/355 nm photoexcitation.

Conclusion

Our results provide evidence for a strong coupling between CNTs and TiO$_2$ in oxMWCNT@TiO$_2$ and of charge separation governed by hole transfer from the valence bands of TiO$_2$ to

MWCNTs. Contrary to the view that MWCNTs always act as electron acceptors when interfaced with TiO$_2$, simulations suggest that metallic SWCNT/TiO$_2$ junctions have a negligible built-in potential of 0.09 eV.[78] Such a small driving force is insufficient to drive any charge separation. Recent simulations using corrected density functional theory methods applied to interfaces formed between graphene and anatase document the benefits of hybridization and the presence of Ti–O–C bonds for interfacial charge transfer. Most importantly, photoexcited electrons are preferentially accumulated in TiO$_2$ whereas holes are predominantly found delocalized in nanocarbon.[46]

In this work, we have demonstrated that ultrafast (<1 ps) hole transfer occurs across the interfaces in oxMWCNT@TiO$_2$ hybrids from the valence bands of TiO$_2$ to the valence bands of oxMWCNTs. Consequently, electrons are accumulated in the conduction bands of TiO$_2$, which is in stark contrast to previous reports. The kinetics of electron–hole recombination across the interface crucially depends on the amount of oxMWCNTs. Our finding suggests that the external surface of TiO$_2$ provides possible active sites of H$_2$ evolution in photocatalytic water splitting in the presence of oxMWCNT@TiO$_2$ hybrids.

Experimental section

Materials

Oxidative functionalization of MWCNTs (oxMWCNT) was performed using the procedure reported elsewhere.[28] Briefly, pristine MWCNTs were sonicated for 5 h with a 3:1 mixture of concentrated H$_2$SO$_4$/HNO$_3$. OxMWCNTs were further characterized by TEM, TGA, and FTIR spectroscopy (not shown). Such a functionalisation enabled adequate dispersibility in solvents and polymer solutions used in the subsequent stages of the synthesis process.

Preparation of fibres

TiO$_2$ and oxMWCNT@TiO$_2$ nanofibres were prepared using sol–gel and electrospinning techniques as reported in earlier work.[28] To prepare the electrospun solution, polyvinyl pyrrolidone (10 wt%) was mixed with ethanol followed by further addition of (63.5%) titanium ethoxide with a few drops of acetic acid added to catalyse the sol–gel formation. For the preparation of oxMWCNT@TiO$_2$ hybrids, oxMWCNTs were dispersed in ethanol by bath sonication (1, 3, and 5 vol%), added to the electrospinning solution, and stirred until homogeneous dispersions were obtained. Then, the solution was loaded in a syringe used for electrospinning (Nanon 01A, MEEC Co., Ltd). A high voltage of 18 kV was applied between the tip and the collector, separated by 10 cm. Nanofibers were electrospun using a precursor feed rate of 2 mL h^{-1} flow and collected over aluminium foil. After electrospinning, the nanofibers were calcined at 400 °C in air for 2.5 h to remove the remaining polymer and subsequently annealed at 500 °C for 1 h to crystallize the titania into predominantly the anatase

phase. This annealing treatment was done under an Ar atmosphere to avoid the degradation of oxMWCNTs.

Characterization techniques

The samples for spectroscopic studies consisted of fibres of TiO_2 and ox-MWCNT@TiO_2 hybrids directly electrospun on quartz, which were subsequently subjected to calcination and annealing processes. The fibres formed a thin layer with a density to match an optical transmittance between 30–70% required for femtosecond transient absorption spectroscopy (TAS) studies.

Morphological characterization of the fibres was performed using a scanning electron microscope at 4–10 keV (SEM, EVO MA15, Zeiss Model) and a high resolution transmission electron microscope (HRTEM, JEOL JEM 3000F) operating at 300 kV. Phase analysis was performed using X-Ray Diffraction (XRD) (Empyrean, PANalytical) using Cu Kα radiation. Raman spectra were obtained with a Renishaw PLC spectrometer with 532 nm wavelength laser-excitation and 1 micron spot size. A laser power of 5.3 mW was used, which we confirmed to be sufficiently low to avoid phase transformation.[79] Interestingly, photoinduced phase transformations were observed upon increasing the laser power as well as by repeated measurements at exactly the same spot (Fig. S1†).

Photoluminescence spectra of solid samples were recorded using a pulsed laser of 355 nm wavelength and repetition rate of 235 Hz for excitation. A cut-off filter at 370 nm was employed to discriminate the laser light and laser-induced luminescence. All measurements were carried out at room temperature. X-ray photoelectron spectroscopy (XPS) data were collected using a SPECS GmBH electron spectroscopy system provided with a PHOIBOS 150+MCD analyser. VB-XPS spectra were obtained with pass energy of 25 eV. Ultraviolet photoelectron spectroscopy (UPS) was performed using a Thermo Scientific Multilab 2000 spectrometer with a 110 mm hemispherical sector analyser. UPS was performed with a He I (21.2 eV) radiation line and a total energy resolution of 200 meV. The energy scale was referenced to the Fermi level measured on a bare Au substrate.

Transient absorption characterization

Femtosecond transient absorption studies were performed with a 258 nm laser source (1 kHz, 150 fs pulse width, output 775 nm) from a titanium sapphire laser (CPA 2110 Laser, Clark-MXR Inc.). The excitation wavelength of 258 nm was produced by the third harmonic generation. The transient absorption spectra were monitored with nanohybrid films on a quartz slide (~1 cm × 3 cm) with a Helios transient absorption spectrometer from ultrafast systems under ambient atmosphere. Raman spectra of samples were collected before and after TAS measurements to ensure that the laser parameters used did not induce structural changes in the sample that could give rise to transient features (Fig. S2†).

Nanosecond transient absorption spectra of colloidal TiO_2 and 1 vol% oxMWCNT@TiO_2 dispersions were performed using a custom built transient absorption spectrometer set-up.

Nanosecond transient absorption laser photolysis measurements were performed with the output from the third harmonic generation (355 nm) of an Nd:YAG laser (Brilliant B, Quantel, output <5 ns, 8 mJ per pulse).

The dispersions were saturated with argon prior to any of the measurements. More details on the instrumentation could be obtained from previous work.[80]

Photocatalytic measurements

For steady state methyl viologen quenching experiments, solutions of 1 mM $[MV]^{2+}2Cl^-$ in D_2O were prepared. About 1 mg ml^{-1} oxMWCNT@TiO_2 dispersion in D_2O was mildly sonicated and transferred to a quartz cuvette. Followed by argon purging for a while, 0.1 ml of 1 mM $[MV]^{2+}2Cl^-$ solution was added to 0.3 ml of nanofibre dispersion. Then, the cuvettes were exposed to UV irradiation (302 nm, 6 Watt) for 20 min. Although steady state photo-oxidation of N,N,N′,N′-tetramethyl-p-phenylenediamine was done in a similar fashion, it was performed under dark conditions and a different irradiation (365 nm, 6 watt) was used. During the transient absorption measurements, both oxMWCNT@TiO_2 dispersions and solutions of electron/hole scavengers were saturated with argon.

Acknowledgements

Notes and references

1 A. Fujishima and K. Honda, *Nature*, 1972, **238**, 37–38.
2 H. Li, Z. Bian, J. Zhu, D. Zhang, G. Li, Y. Huo, H. Li and Y. Lu, *J. Am. Chem. Soc.*, 2007, **129**, 8406–8407.
3 A. A. Ismail and D. W. Bahnemann, *J. Mater. Chem.*, 2011, **21**, 11686–11707.
4 N. K. Shrestha, J. M. Macak, F. Schmidt-Stein, R. Hahn, C. T. Mierke, B. Fabry and P. Schmuki, *Angew. Chem., Int. Ed.*, 2009, **48**, 969–972.
5 D. Li and Y. Xia, *Nano Lett.*, 2003, **3**, 555–560.
6 S. K. Choi, S. Kim, J. Ryu, S. K. Lim and H. Park, *Photochem. Photobiol. Sci.*, 2012, **11**, 1437–1444.
7 A. Ivanova, D. Fattakhova-Rohlfing, B. E. Kayaalp, J. Rathouský and T. Bein, *J. Am. Chem. Soc.*, 2014, **136**, 5930–5937.
8 H. Zhang, M. P. Finnegan and J. F. Banfield, *Nanoscale*, 2013, **5**, 6742–6746.
9 K.-T. Kim, G. Ali, K. Y. Chung, C. S. Yoon, H. Yashiro, Y.-K. Sun, J. Lu, K. Amine and S.-T. Myung, *Nano Lett.*, 2014, **14**, 416–422.

10 M. I. Dar, F. J. Ramos, Z. Xue, B. Liu, S. Ahmad, S. A. Shivashankar, M. K. Nazeeruddin and M. Grätzel, *Chem. Mater.*, 2014, **26**, 4675–4678.

11 O. Carp, C. L. Huisman and A. Reller, *Prog. Solid State Chem.*, 2004, **32**, 33–177.

12 P. S. Archana, R. Jose, C. Vijila and S. Ramakrishna, *J. Phys. Chem. C*, 2009, **113**, 21538–21542.

13 D. C. Hurum, A. G. Agrios, K. A. Gray, T. Rajh and M. C. Thurnauer, *J. Phys. Chem. B*, 2003, **107**, 4545–4549.

14 A. Kafizas, X. Wang, S. R. Pendlebury, P. Barnes, M. Ling, C. Sotelo-Vazquez, R. Quesada-Cabrera, C. Li, I. P. Parkin and J. R. Durrant, *J. Phys. Chem. A*, 2016, **120**, 715–723.

15 D. O. Scanlon, C. W. Dunnill, J. Buckeridge, S. A. Shevlin, A. J. Logsdail, S. M. Woodley, C. R. A. Catlow, M. J. Powell, R. G. Palgrave, I. P. Parkin, G. W. Watson, T. W. Keal, P. Sherwood, A. Walsh and A. A. Sokol, *Nat. Mater.*, 2013, **12**, 798–801.

16 L. Matějová, K. Kočí, M. Reli, L. Čapek, A. Hospodková, P. Peikertová, Z. Matěj, L. Obalová, A. Wach, P. Kuśtrowski and A. Kotarba, *Appl. Catal., B*, 2014, **152**, 172–183.

17 B. Liu, H. M. Chen, C. Liu, S. C. Andrews, C. Hahn and P. Yang, *J. Am. Chem. Soc.*, 2013, **135**, 9995–9998.

18 A. A. Murashkina, P. D. Murzin, A. V. Rudakova, V. K. Ryabchuk, A. V. Emeline and D. W. Bahnemann, *J. Phys. Chem. C*, 2015, **119**, 24695–24703.

19 X. Qiu, M. Miyauchi, K. Sunada, M. Minoshima, M. Liu, Y. Lu, D. Li, Y. Shimodaira, Y. Hosogi, Y. Kuroda and K. Hashimoto, *ACS Nano*, 2012, **6**, 1609–1618.

20 H. Tada, Q. Jin, A. Iwaszuk and M. Nolan, *J. Phys. Chem. C*, 2014, **118**, 12077–12086.

21 D. Mitoraj and H. Kisch, *Angew. Chem., Int. Ed.*, 2008, **47**, 9975–9978.

22 R. Asahi, T. Morikawa, H. Irie and T. Ohwaki, *Chem. Rev.*, 2014, **114**, 9824–9852.

23 C. Yang, Z. Wang, T. Lin, H. Yin, X. Lü, D. Wan, T. Xu, C. Zheng, J. Lin, F. Huang, X. Xie and M. Jiang, *J. Am. Chem. Soc.*, 2013, **135**, 17831–17838.

24 M. V. Dozzi and E. Selli, *J. Photochem. Photobiol., C*, 2013, **14**, 13–28.

25 J. Liu, Q. Zhang, J. Yang, H. Ma, M. O. Tade, S. Wang and J. Liu, *Chem. Commun.*, 2014, **50**, 13971–13974.

26 K. J. Williams, C. A. Nelson, X. Yan, L.-S. Li and X. Zhu, *ACS Nano*, 2013, **7**, 1388–1394.

27 D. Eder and A. H. Windle, *Adv. Mater.*, 2008, **20**, 1787–1793.

28 A. Moya, A. Cherevan, S. Marchesan, P. Gebhardt, M. Prato, D. Eder and J. J. Vilatela, *Appl. Catal., B*, 2015, **179**, 574–582.

29 K. Woan, G. Pyrgiotakis and W. Sigmund, *Adv. Mater.*, 2009, **21**, 2233–2239.

30 N. Yang, Y. Liu, H. Wen, Z. Tang, H. Zhao, Y. Li and D. Wang, *ACS Nano*, 2013, **7**, 1504–1512.

31 W. Wang, P. Serp, P. Kalck and J. L. Faria, *J. Mol. Catal. A: Chem.*, 2005, **235**, 194–199.

32 C. J. Shearer, A. Cherevan and D. Eder, *Adv. Mater.*, 2014, **26**, 2295–2318.

33 J. E. Weaver, M. R. Dasari, A. Datar, S. Talapatra and P. Kohli, *ACS Nano*, 2010, **4**, 6883–6893.

34 G. D. M. R. Dabera, K. D. G. I. Jayawardena, M. R. R. Prabhath, I. Yahya, Y. Y. Tan, N. A. Nismy, H. Shiozawa, M. Sauer, G. Ruiz-Soria, P. Ayala, V. Stolojan, A. A. D. T. Adikaari, P. D. Jarowski, T. Pichler and S. R. P. Silva, *ACS Nano*, 2013, **7**, 556–565.

35 N. M. Dissanayake and Z. Zhong, *Nano Lett.*, 2011, **11**, 286–290.

36 S. Ren, M. Bernardi, R. R. Lunt, V. Bulovic, J. C. Grossman and S. Gradečak, *Nano Lett.*, 2011, **11**, 5316–5321.

37 S. Banerjee and S. S. Wong, *Nano Lett.*, 2002, **2**, 195–200.

38 K. Jung, J. S. Hong, R. Vittal and K.-J. Kim, *Chem. Lett.*, 2002, **31**, 864–865.

39 Y. Wei, H. Du, J. Kong, X. Lu, L. Ke and X. W. Sun, *Electrochim. Acta*, 2014, **143**, 188–195.

40 J. J. Vilatela and D. Eder, *ChemSusChem*, 2012, **5**, 456–478.

41 H. Chong, G. Wei, H. Hou, H. Yang, M. Shang, F. Gao, W. Yang and G. Shen, *Nano Res.*, 2015, **8**, 2822–2832.

42 A. Molina-Mendoza, A. Moya, R. Frisenda, S. A. Svatek, P. Gant, S. Gonzalez-Abad, E. Antolin, N. Agrait, G. R. Bollinger, D. Perez de Lara, J. Vilatela and A. Castellanos-Gomez, *J. Mater. Chem. C*, 2016, **4**, 10707–10714.

43 F. H. Bijarbooneh, Y. Zhao, Z. Sun, Y.-U. Heo, V. Malgras, J. H. Kim and S. X. Dou, *APL Mater.*, 2013, **1**, 032106.

44 N. K. Eswar, P. C. Ramammurthy and G. Madras, *New J. Chem.*, 2015, **39**, 6040–6051.

45 K.-R. Zhu, M.-S. Zhang, Q. Chen and Z. Yin, *Phys. Lett. A*, 2005, **340**, 220–227.

46 L. Ferrighi, G. Fazio and C. D. Valentin, *Adv. Mater. Interfaces*, 2016, **3**, 1500624.

47 R. J. Young, I. A. Kinloch, L. Gong and K. S. Novoselov, *Compos. Sci. Technol.*, 2012, **72**, 1459–1476.

48 J. E. Lee, G. Ahn, J. Shim, Y. S. Lee and S. Ryu, *Nat. Commun.*, 2012, **3**, 1024.

49 A. Das, S. Pisana, B. Chakraborty, S. Piscanec, S. K. Saha, U. V. Waghmare, K. S. Novoselov, H. R. Krishnamurthy, A. K. Geim, A. C. Ferrari and A. K. Sood, *Nat. Nanotechnol.*, 2008, **3**, 210–215.

50 C. C. Mercado, F. J. Knorr, J. L. McHale, S. M. Usmani, A. S. Ichimura and L. V. Saraf, *J. Phys. Chem. C*, 2012, **116**, 10796–10804.

51 Z. Zhang and J. T. Yates, *Chem. Rev.*, 2012, **112**, 5520–5551.

52 S. Farsinezhad, H. Sharma and K. Shankar, *Phys. Chem. Chem. Phys.*, 2015, **17**, 29723–29733.

53 H. Ago, T. Kugler, F. Cacialli, W. R. Salaneck, M. S. P. Shaffer, A. H. Windle and R. H. Friend, *J. Phys. Chem. B*, 1999, **103**, 8116–8121.

54 R. Gao, Z. Pan and Z. L. Wang, *Appl. Phys. Lett.*, 2001, **78**, 1757–1759.

55 S. Gutmann, M. A. Wolak, M. Conrad, M. M. Beerbom and R. Schlaf, *J. Appl. Phys.*, 2010, **107**, 113719.

56 G. Xiong, R. Shao, T. C. Droubay, A. G. Joly, K. M. Beck, S. A. Chambers and W. P. Hess, *Adv. Funct. Mater.*, 2007, **17**, 2133–2138.

57 C.-F. Chi, H.-W. Cho, H. Teng, C.-Y. Chuang, Y.-M. Chang, Y.-J. Hsu and Y.-L. Lee, *Appl. Phys. Lett.*, 2011, **98**, 012101.

58 S. Kumar, C. Mukherjee and D. M. Phase, 2014, arXiv E-Prints.

59 Y. Park, W. Kim, D. Monllor-Satoca, T. Tachikawa, T. Majima and W. Choi, *J. Phys. Chem. Lett.*, 2013, **4**, 189–194.

60 T. An, J. Chen, X. Nie, G. Li, H. Zhang, X. Liu and H. Zhao, *ACS Appl. Mater. Interfaces*, 2012, **4**, 5988–5996.

61 X. Pan, Y. Zhao, S. Liu, C. L. Korzeniewski, S. Wang and Z. Fan, *ACS Appl. Mater. Interfaces*, 2012, **4**, 3944–3950.

62 N. Lakshminarasimhan, W. Kim and W. Choi, *J. Phys. Chem. C*, 2008, **112**, 20451–20457.

63 M. Xing, F. Shen, B. Qiu and J. Zhang, *Sci. Rep.*, 2014, **4**, 6341.

64 Y. Sun, J. Zhu, L. Bai, Q. Li, X. Zhang, W. Tong and Y. Xie, *Inorg. Chem. Front.*, 2014, **1**, 58–64.

65 S. Ayissi, P. A. Charpentier, K. Palotás, N. Farhangi, F. Schwarz and W. A. Hofer, *J. Phys. Chem. C*, 2015, **119**, 15085–15093.

66 A. Furube, T. Asahi, H. Masuhara, H. Yamashita and M. Anpo, *J. Phys. Chem. B*, 1999, **103**, 3120–3127.

67 D. Bahnemann, A. Henglein, J. Lilie and L. Spanhel, *J. Phys. Chem.*, 1984, **88**, 709–711.

68 T. Yoshihara, R. Katoh, A. Furube, Y. Tamaki, M. Murai, K. Hara, S. Murata, H. Arakawa and M. Tachiya, *J. Phys. Chem. B*, 2004, **108**, 3817–3823.

69 A. Kahnt, C. Oelsner, F. Werner, D. M. Guldi, S. P. Albu, R. Kirchgeorg, K. Lee and P. Schmuki, *Appl. Phys. Lett.*, 2013, **102**, 233109.

70 X. Yang and N. Tamai, *Phys. Chem. Chem. Phys.*, 2001, **3**, 3393–3398.

71 P. Zawadzki, *J. Phys. Chem. C*, 2013, **117**, 8647–8651.

72 A likely rational for such a negative transient is emission upon photoexcitation as we can exclude ground state absorption and scattering based on temporal resolution of our spectrometer.

73 R. B. Draper and M. A. Fox, *Langmuir*, 1990, **6**, 1396–1402.

74 F. J. Rawson, A. J. Downard and K. H. Baronian, *Sci. Rep.*, 2014, **4**, 5216.

75 T. Watanabe and K. Honda, *J. Phys. Chem.*, 1982, **86**, 2617.

76 E. Borgarello, E. Pelizzetti, W. A. Mulac and D. Meisel, *J. Chem. Soc., Faraday Trans. 1*, 1985, **81**, 143–159.

77 D. Dung, J. Ramsden and M. Graetzel, *J. Am. Chem. Soc.*, 1982, **104**, 2977–2985.

78 R. Long, *J. Phys. Chem. Lett.*, 2013, **4**, 1340–1346.

79 G. C. Vásquez, M. A. Peche-Herrero, D. Maestre, A. Gianoncelli, J. Ramírez-Castellanos, A. Cremades, J. M. González-Calbet and J. Piqueras, *J. Phys. Chem. C*, 2015, **119**, 11965–11974.

80 A. Kahnt, L.-P. Heiniger, S.-X. Liu, X. Tu, Z. Zheng, A. Hauser, S. Decurtins and D. M. Guldi, *ChemPhysChem*, 2010, **11**, 651–658.